JACS
JOURNAL OF THE AMERICAN CHEMICAL SOCIETY
Article
pubs.acs.org/JACS

Structural Complexity Meets Transport and Magnetic Anisotropy in Single Crystalline $Ln_{30}Ru_4Sn_{31}$ (Ln = Gd, Dy)

Devin C. Schmitt,[†] Neel Haldolaarachchige,[‡] Joseph Prestigiacomo,[‡] Amar Karki,[‡] David P. Young,[‡] Shane Stadler,[‡] Rongying Jin,[‡] and Julia Y. Chan*,[†]

[†]Department of Chemistry and [‡]Department of Physics and Astronomy, Louisiana State University, Baton Rouge, Louisiana 70803, United States

Ⓢ Supporting Information

ABSTRACT: We present the structure of $Ln_{30}Ru_{4+x}Sn_{31-y}$ (Ln = Gd, Dy) and the anisotropic resistivity, magnetization, thermopower, and thermal conductivity of single crystal $Ln_{30}Ru_{4+x}Sn_{31-y}$ (Ln = Gd, Tb). $Gd_{30}Ru_{4.92}Sn_{30.54}$ crystallizes in a new structure-type with space group *Pnnm* and dimensions of a = 11.784(1) Å, b = 24.717(1) Å, and c = 11.651(2) Å, and V = 3394(1) Å^3. Magnetic anisotropy and highly anisotropic electrical transport behavior were observed in the single crystals of $Gd_{30}Ru_{4.92}Sn_{30.54}$ and $Tb_{30}Ru_6Sn_{29.5}$. Additionally, the lattice thermal conductivity of $Tb_{30}Ru_6Sn_{29.5}$ is quite low, and a comparison is made to other Sn-containing compounds.

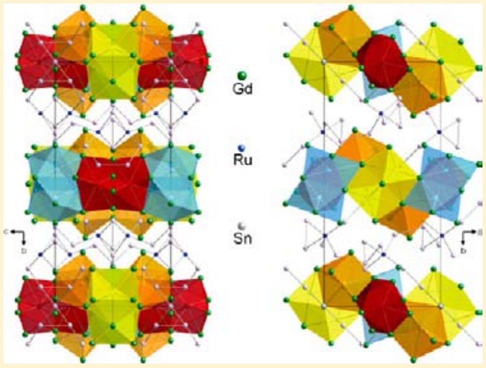

INTRODUCTION

Intermetallic compounds display a variety of useful bulk properties, including magnetocaloric effects, superconductivity, and thermoelectric behavior. For instance, $Gd_5Si_2Ge_2$ displays a giant magnetocaloric effect near room temperature.[1] MgB_2[2] and $Ba_{0.6}K_{0.4}Fe_2As_2$[3] are oxygen-free materials that have been shown to be superconductors near 40 K, and low-temperature properties, such as unconventional superconductivity, heavy fermion behavior, and exotic magnetism, have also been observed in a variety of intermetallic compounds.[4] Additionally, intermetallic compounds, such as Zn_4Sb_3[5] and $Yb_{14}MnSb_{11}$,[6] exhibit exemplary physical properties for thermoelectric applications.

Anisotropic properties of intermetallic materials are less studied, since high-quality, sizable single crystals are necessary for these measurements. This precludes the use of popular synthetic methods, such as arc melting and ball milling, which produce polycrystalline products. Single crystals must also be oriented along crystallographic directions using, for example, Laue diffraction before anisotropic physical property measurements can be performed. Moreover, the macroscopic geometry of the crystals is important in transport property measurements that are highly influenced by crystal shape and size, such as electrical resistivity, thermopower, and thermal conductivity. Thus, measurement of a well-shaped crystal, such as a polished bar, is ideal, while crystals with shorter macroscopic axes, such as needles and plates, can introduce significant experimental error when measuring along the short axis. Anisotropic magnetic properties, however, are more common, as the macroscopic crystal shape typically has a less pronounced effect on experimental error.

Despite these difficulties, anisotropic physical properties measurements have been reported for a number of intermetallic systems in an effort to study complex electrical and magnetic phenomena. For example, anisotropic magnetization measurements have been performed for several intermetallic compounds, including Eu_3InP_3[7] and $EuGa_2P_2$,[8] which show multiple field-direction-dependent magnetic ordering transitions. Polycrystalline $Ce_3Cu_4Sn_4$ exhibits multiple magnetic ordering events in temperature-dependent magnetization data, and fits from neutron data confirm the coexistence of two anisotropic magnetic sublattices corresponding to the two crystallographically unique Ce positions.[9] Giant and highly anisotropic magnetocaloric effects have been observed in the magnetocaloric material $EuFe_2As_2$ at T = 20 K.[10] Though less common, many examples of anisotropic intermetallic electrical properties exist. $Al_{72.5}Mn_{21.5}Fe_{6.0}$ exhibits anisotropic electrical resistivity but was found to have a nearly isotropic Fermi surface with the resistivity differences caused by anisotropic quenched defect scattering,[11] while the origin of the highly electrically anisotropic *d*-Al−Co−Ni decagonal quasicrystalline phase was found to be a highly anisotropic Fermi surface.[12] Other notable examples of intermetallics displaying anisotropic electrical properties include the high-temperature Kondo systems URu_2Si_2[13] and $CePt_2In_7$,[14] and the iron−arsenide superconducting compounds $BaFe_2As_2$[15] and $CaFe_4As_3$.[16]

We have recently reported on the exceptionally low lattice thermal conductivity (κ_L = 0.28 W/m·K) and unusual semiconducting-like transport behavior of $Gd_{117}Co_{56}Sn_{112}$.[17] A

Received: December 3, 2012
Published: January 25, 2013

Table 1. Crystallographic Parameters for $Ln_{30}Ru_{4+2x}Sn_{31-x}$ (Ln= Gd, Dy) and $Tb_{30}Ru_{6.0}Sn_{29.5}$

formula	$Gd_{30}Ru_{4.92(5)}Sn_{30.54(9)}$	$Tb_{30}Ru_{6.0(4)}Sn_{29.5(7)}$	$Dy_{30}Ru_{4.57(5)}Sn_{30.72(9)}$
crystal system	orthorhombic	orthorhombic	orthorhombic
space group	*Pnnm*	*Pnnm*	*Pnnm*
a (Å)	11.784(1)	11.696(1)	11.659(1)
b(Å)	24.717(1)	24.505(1)	24.457(1)
c (Å)	11.651(2)	11.578(2)	11.564(2)
V (Å^3)	3393.5(7)	3318.4(7)	3297.4(7)
Z	2	2	2
crystal dimensions (mm^3)	0.05 × 0.05 × 0.05	0.03 × 0.03 × 0.05	0.05 × 0.05 × 0.05
temperature (K)	296(1)	296(1)	296(1)
θ range (°)	4.11−31.00	4.15−30.99	4.16−30.99
μ (mm^{-1})	40.872	43.63	45.872
measured reflections	76592	71549	84140
unique reflections	5622	5502	5469
reflections with I > 2σ(I)	4762	4865	4368
R_{int}	0.0248	0.0181	0.0307
h	−17 to 17	−16 to 16	−16 to 16
k	−35 to 35	−35 to 35	−35 to 35
l	−16 to 16	−16 to 16	−16 to 16
$\Delta\rho_{max}$ (eÅ^{-3})/$\Delta\rho_{min}$ (eÅ^{-3})	2.525/−2.391	2.19/−1.643	3.407/−2.339
GoF	1.287	1.29	1.101
extinction coefficient	0.000111(5)	0.000133(4)	0.000200(6)
reflections/parameters	5622/183	5502/181	5469/183
R_1 ($F^2 > 2\sigma F^2$)^a	0.0288	0.023	0.0291
wR_2 (F^2)^b	0.0605	0.0436	0.0539

$^a R_1 = \sum|Fo| - |Fc|/\sum|Fo|$. $^b wR_2 = [\sum[w(F_o^2 - F_c^2)]/\sum[w(F_o^2)^2]]^{1/2}$.

similar growth technique was employed, using the self-flux method, in an effort to synthesize a Ru analogue. Instead, we found that single crystals of a highly complex rare earth-rich structure form with a new structure-type, which crystallizes in the orthorhombic space group *Pnnm* with a total of 24 crystallographically unique atomic sites and 11 magnetic rare earth sites. With the large number of magnetic sites comes the potential for multiple magnetic sublattices in the structure. Herein, we report on the growth and crystal structure of $Gd_{30}Ru_{4.92}Sn_{30.54}$, $Tb_{30}Ru_6Sn_{29.5}$, and $Dy_{30}Ru_{4.57}Sn_{30.72}$ as well as the magnetic, electronic, and thermal transport properties of single crystal $Gd_{30}Ru_{4.92}Sn_{30.54}$ and $Tb_{30}Ru_6Sn_{29.5}$. We found both magnetic anisotropy and highly anisotropic electrical transport behavior. Additionally, we found that the lattice thermal conductivity in $Tb_{30}Ru_6Sn_{29.5}$ is exceptionally low, and we compare our results to other Sn-containing materials.

■ EXPERIMENTAL SECTION

Synthesis. Ru powder, Sn shot, and ingots of Gd, Tb, and Dy (all ≥99.9 wt % purity, metal basis) were used for the preparation of $Ln_{30}Ru_{4+x}Sn_{31-y}$ ($x = 0.57-2.0$, $y = 0.28-1.5$). Elements were weighed out using a molar ratio of 12:6:11 (Ln:Ru:Sn), placed into an alumina crucible, and loaded into a fused silica tube which was evacuated (~1.2 × 10^{-3} atm). The total mass of starting material used in a typical reaction was ~1.5g. The addition of excess Sn results in the formation of $LnRuSn_2$ with the $CeNiSi_2$ structure type.[18] The tubes were subsequently backfilled with ~0.2 atm Ar (to prevent fused silica tube collapse due to high maximum dwell temperatures) and were sealed. The reaction vessels were heated to 1260 °C at 100 °C/h, held at 1260 °C for 36 h, cooled at 1 °C/h to 1200 °C, and cooled at 5 °C/h to 1050 °C. The samples were then removed from the furnace and allowed to cool in air or quenched in water. Single crystals of $Ln_{30}Ru_{4+x}Sn_{31-y}$ were embedded in buttons of polycrystalline material typically consisting of multiple binary phases (including, in the case of the Gd analogue, $RuSn_2$, Gd_5Ru_2, Gd_2Ru, Gd_3Ru, and $GdRu_2$). Reactions were later carried out using a starting molar ratio of 12:4.75−5.25:11, which resulted in higher yields of the title compounds, with identical crystalline stoichiometries. The title compounds all exhibit a dark gray or black color with metallic luster which is easily distinguishable from the surrounding polycrystalline matrix. Yields for the targeted phases were found to be the highest for the Tb analogue, with Tb > Gd > Dy. The single crystals were highly reactive with HNO_3, HCl, and H_2SO_4; thus, mechanical extraction was necessary to separate the single crystals from the surrounding polycrystalline matrix.

Elemental Analysis. Elemental analysis was performed using energy dispersive X-ray spectroscopy using a FEI Quanta 200 scanning electron microscope with an accelerating voltage of 20 keV. At least six points per sample were averaged together for each stoichiometric determination. Ru concentration showed little deviated (within instrumental error) between data points of individual analogues, indicating high sample homogeneity. The measured compositions of the samples were $Gd_{30(3)}Ru_{6(3)}Sn_{31(2)}$, $Tb_{30(3)}Ru_{7(2)}Sn_{32(3)}$, and $Dy_{30(3)}Ru_{6(2)}Sn_{33(2)}$. Error bars were determined by summing a fixed 3 atomic % instrumental error and the standard deviations of the data collected.

X-ray Diffraction. Powder X-ray diffraction was performed to determine homogeneity and phase purity using a Bruker D8 Advance X-ray diffractometer with monochromatic Cu Kα radiation with an incident beam Ge monochromator. Data were collected from 10−80 2θ with a resolution of 0.01°. Single crystal X-ray diffraction data were collected using a Nonius KappaCCD diffractometer with monochromatic Mo Kα radiation. Single crystals were cut to appropriate sizes (Table 1) and mounted to a glass fiber using epoxy. All data were collected with high redundancy, and a multiscan absorption correction was applied during the scaling process. Overall R_{merge} values during scaling were less than 0.091 for all analogues. Statistics suggested that the structure was centrosymmetric. Systematic absences ($h0l$: $h + l = 2n$; $hk0$: $h + k = 2n$; $h00$: $h = 2n$; $0k0$: $k = 2n$; $00l$: $l = 2n$) allowed for several possible space groups and indicated *n* glide planes in the *b* and *c* directions. Solutions were attempted in direct methods using SIR2002[19] in space groups with similar systematic absences (*Pnnn*, *Pnna*, *Pccn*, *Pmmn*, *Pbcn*, and *Pnma*), none of which returned valid solutions. Space groups *P2nn* and *Pmnn* were solved using SIR2002[19]

Table 2. Positions, Occupancies, And Atomic Displacement Parameters for $Gd_{30}Ru_{4.92}Sn_{30.54}$

atom	site	x	y	z	occ.	U_{eq} (Å^2)[a]
Gd1	4g	0.14000(5)	0.65899(2)	0	1	0.00981(11)
Gd2	4g	0.59006(5)	0.89950(2)	0	1	0.00920(11)
Gd3	4g	0.26447(5)	0.96935(2)	0	1	0.00885(11)
Gd4	4g	0.78306(5)	0.80299(2)	0	1	0.01078(12)
Gd5	4*e*	0	0	0.26566(5)	1	0.00854(11)
Gd6	4g	0.32790(5)	0.41893(2)	0	1	0.01155(12)
Gd7	8h	0.43894(3)	0.652434(16)	0.81903(3)	1	0.00944(8)
Gd8	8h	0.82070(3)	0.473690(16)	0.17546(3)	1	0.00894(8)
Gd9	8h	0.73377(3)	0.720426(17)	0.26051(3)	1	0.01068(8)
Gd10	8h	0.42987(3)	0.884470(17)	0.25974(3)	1	0.00924(8)
Gd11[b]	4g	0.93660(14)	0.14080(7)	0	0.770(4)	0.0118(3)
Gd11′ [b]	4g	0.9328(5)	0.1252(2)	0	0.230(4)	0.0118(3)
Ru1	8h	0.51113(5)	0.78813(3)	0.12548(5)	1	0.00885(12)
Ru2′ [b]	4g	0.1317(4)	0.77393(18)	0	0.230(4)	0.0138(13)
Sn1	4f	0	0.5	0.36253(7)	1	0.00877(15)
Sn2	2a	0	0	0	1	0.0126(2)
Sn3	4g	0.35287(7)	0.84934(3)	0	1	0.01106(16)
Sn4	8h	0.83726(4)	0.92164(2)	0.12547(5)	1	0.00891(11)
Sn5	4g	0.34431(7)	0.73615(3)	0	1	0.01049(16)
Sn6	4g	0.60752(7)	0.70727(3)	0	1	0.01040(15)
Sn7	4g	0.62030(7)	0.44466(3)	0	1	0.01017(15)
Sn8	4g	0.95965(7)	0.55678(3)	0	1	0.01067(16)
Sn9	8h	0.67358(4)	0.59207(2)	0.26393(5)	1	0.01020(11)
Sn10	8h	0.67739(4)	0.84521(2)	0.23564(5)	1	0.00810(11)
Sn11[b]	8h	0.9851(6)	0.7487(3)	0.8451(7)	0.770(4)	0.0098(5)
Sn11′ [b]	8h	0.976(2)	0.7442(11)	0.840(3)	0.230(4)	0.0098(5)
Sn12[b]	4g	0.8549(6)	0.67532(16)	0	0.770(4)	0.0096(5)
Ru12′ [b]	4g	0.859(3)	0.6833(8)	0	0.230(4)	0.0096(5)

[a] U_{eq} is defined as one-third of the trace of the orthogonalized U_{ij} tensor. [b] Positional and/or occupational disorder of Gd11, Sn11, and Sn12 with Gd11′, Sn11′, and Ru12′, respectively. Ru2′ occurs at the same frequency as the disordered atoms.

and refined using SHELXL97.[20] An analysis of the refined model in space group *P*2*nn* using Platon[21] indicated missing mirror plane symmetry elements; thus, *Pmnn* was used for all model refinements. Since *Pmnn* corresponded to a nonstandard space group setting, the data were transformed to the standard space group setting of *Pnnm*. Crystallographic and atomic parameters are provided in Tables 1 and 2, respectively. Atomic parameters for $Tb_{30}Ru_6Sn_{29.5}$ and $Dy_{30}Ru_{4.57}Sn_{30.72}$ are provided in Table S1. It should be noted that data collected from different crystals from batches (and between batches of the same analogues) were modeled to stoichiometries within experimental error, indicating high sample homogeneity.

Modeling Structural Disorder. Several positionally disordered atomic sites linked to the occupancy of the Ru2′ atom were found while refining the model. A detailed explanation of the disorder modeling can be found in Supporting Information (SI). The primed (Ru2′, Sn11′, Ru12′, and Gd11′) and nonprimed (Sn11, Sn12, and Gd11) atoms listed in Table 2 always occur as a group. The two possible configurations of positional disorder, depending upon the existence of Ru2′, are shown in Figure 1. The Gd and Dy analogues display the same trend in positional disorder with occupancy splitting of 77:23 and 86:14, of Sn12:Ru12′, respectively. However, the Tb analogue shows the opposite mixing ratio with 24:76 of Sn12′:Ru12, which is consistent with our elemental analysis data showing a higher Ru content in the Tb analogue relative to the Gd and Dy analogues. Additionally, there was insufficient evidence to support Sn12′/Ru12 site splitting in the Tb analogue; thus, the Sn12′/Ru12 site was modeled as a single mixed site for the Tb analogue. Atomic positions, occupancies, and atomic displacement parameters are provided in Table 2. The higher probability configuration of the 77:23 disordered splitting for the Gd analogue, shown in Figure 1c, is used for all structural modeling.

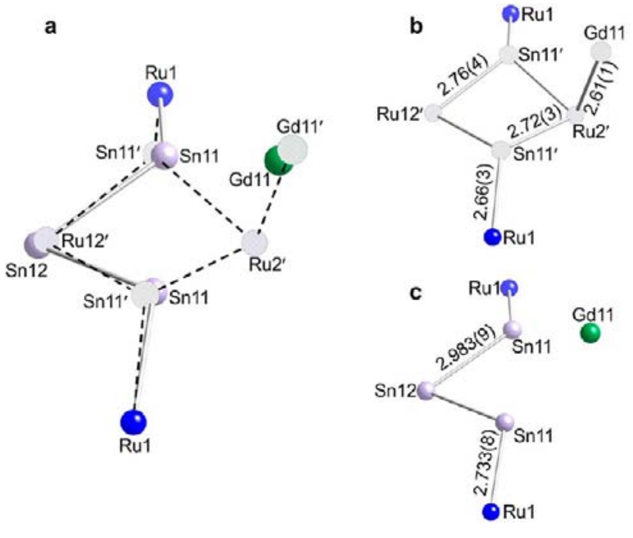

Figure 1. Positionally disordered model of $Gd_{30}Ru_{4.92}Sn_{30.54}$ showing (a) all disordered atoms, (b) lower occupancy disordered atoms, and (c) higher occupancy disordered atoms. Additional atoms adjacent to Ru12′/Sn12, Ru1, and Ru2′ have been omitted for clarity.

Physical Properties. Single crystals were oriented using single crystal X-ray diffraction prior to physical property measurements. A single crystal of $Tb_{30}Ru_6Sn_{29.5}$ was polished to a bar shape of approximately 1 × 1 × 2.5 mm^3 for resistivity and thermal conductivity measurements. Temperature and field-dependent measurements were performed using either a quantum design physical property measurement system (PPMS) or a quantum design magnetic property

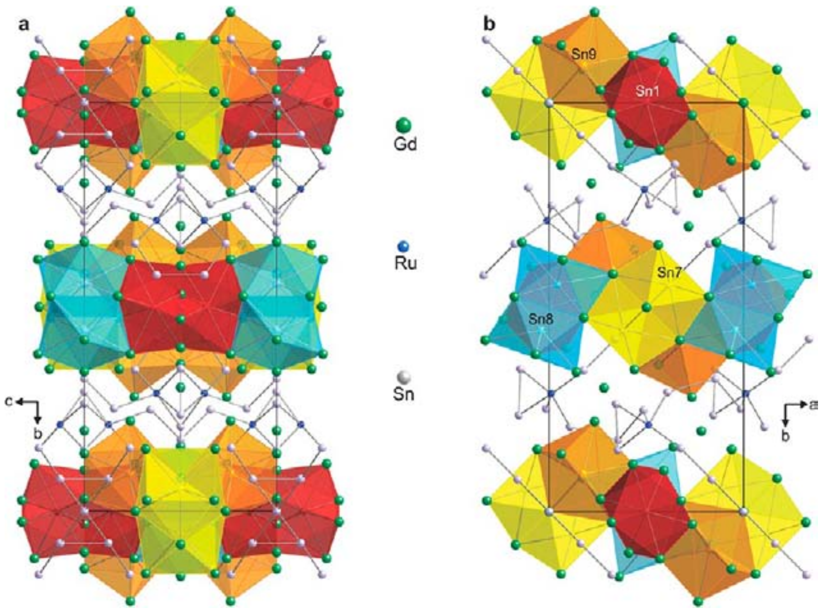

Figure 2. Crystal structure of $Gd_{30}Ru_{4.92}Sn_{30.54}$ shown along the (a) *a*-axis and (b) *c*-axis.

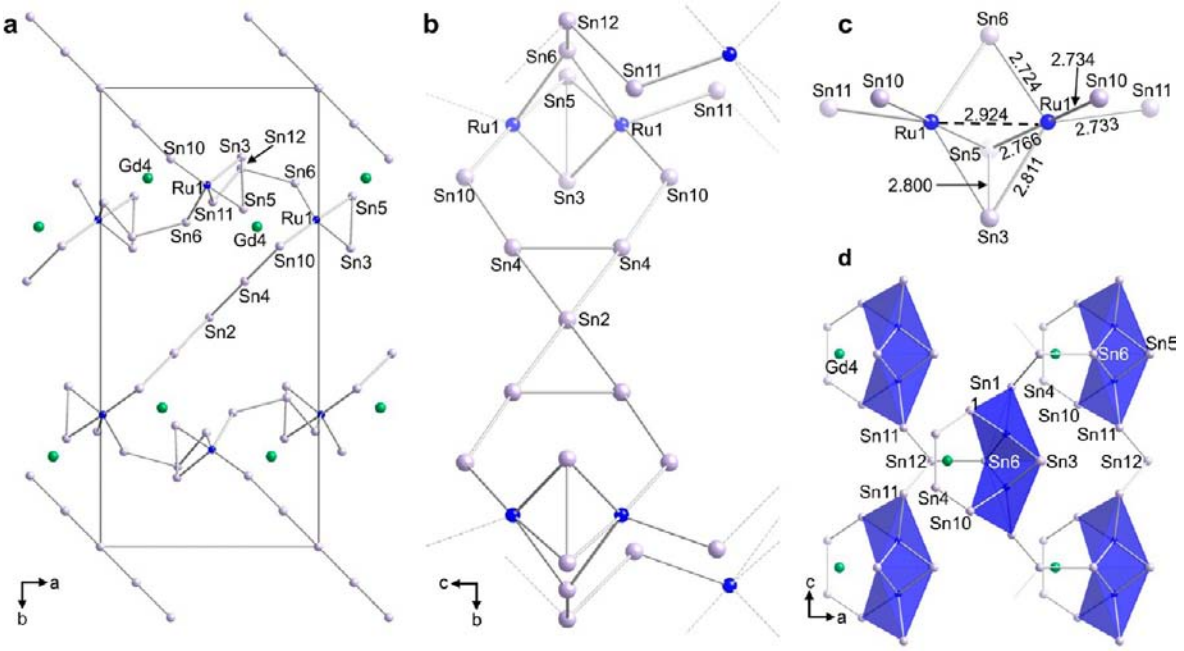

Figure 3. (a) Ru−Sn/Sn−Sn framework in $Gd_{30}Ru_{4.92}Sn_{30.54}$ shown down the *c*-axis. (b) Interpenetrating framework of Sn centered about Sn2. (c) A pair of Ru1 bonding units and (d) one layer of Ru1 bonding units shown down the *b*-axis. The central Ru1 bonding unit is in-plane, and the four flanking bonding units are below the plane.

measurement system in fields of 0−9 T. Temperature-dependent electrical resistivity and Seebeck coefficient were measured in the PPMS using a standard four-probe method and using a comparative technique with a constantine standard, respectively. Thermal conductivity from 172−305 K was directly measured in the PPMS using a standard two-probe method.

RESULTS AND DISCUSSION

Crystal Structure. The two basic criteria that were considered when depicting an accurate structural representation of $Gd_{30}Ru_{4.92}Sn_{30.54}$ were that every atom in the structure must be represented and that the bonds and the arrangement of atoms in the structure must be chemically reasonable. As such, it was found that the interatomic forces present in the crystal structure could not be completely described as ionic (or Zintl) or covalent in nature; rather, the bonding displays both Zintl-like and covalent characteristics.

The crystal structure of $Gd_{30}Ru_{4.92}Sn_{30.54}$ is shown in Figure 2 and is composed of Gd-rich slabs and a Gd-poor framework in the *a*−*c* plane that stack in the *b*-direction. The Gd-poor framework shows infinite Ru−Sn and Sn−Sn bonding networks in the *a*−*c* planes and forms an interpenetrating Sn net through the Gd-rich slabs. The Gd-rich slabs contain Gd surrounding lone Sn or single-bonded dumbell Sn−Sn atoms, similar to that in $Ca_{36}Sn_{23}$[22] and the Zintl phases $Yb_{36}Sn_{23}$[23] and $Ca_{31}Sn_{20}$.[24,25] We therefore adopt a Sn-centered ($Sn@Gd_8$) polyhedral model

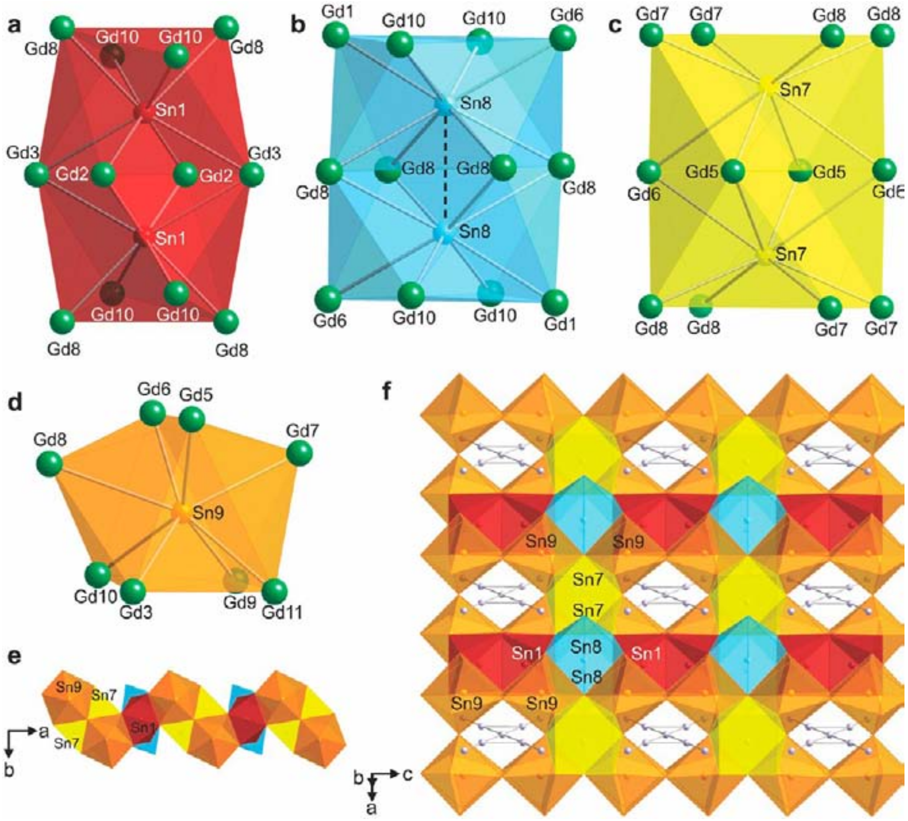

Figure 4. Sn@Gd_8 polyhedral units showing (a) Sn1@Gd_8 confacial distorted square antiprisms, (b) Sn8@Gd_8 confacial distorted square antiprisms, (c) Sn7@Gd_8 confacial square antiprisms, and a (d) Sn9@Gd_8 bicapped trigonal prism. The Sn12 atoms situated above and below the Sn8 polyhedra are omitted for clarity. (e) Zig-zag chain of Sn@Gd_8 polyhedra shown down the *c*-axis. (f) Plane of Sn@Gd_8 polyhedra with interpenetrating framework (Gd atoms and Sn−Gd bonds are omitted in e and f for clarity).

for the Gd-rich slabs, as they show similar features to the Zintl phases listed above. Here, the shorthand X@Y_z is used, where X is the central atom of the polyhedron, Y is the surrounding atom(s), and *z* is the number of Y atoms surrounding X. The slabs and framework can be regenerated by performing a 2_1 screw-axis symmetry operation in the stacking direction (*b*-axis) at 1/4 0 1/4, a 2_1 symmetry operation along the *a*-axis at 0 1/4 1/4, or a mirror in the *c*-direction.

The Gd-poor regions, shown in Figure 3, contain a Ru−Sn/Sn−Sn framework. The framework can be conveniently described by a planar Sn−Sn net interpenetrating the Sn@Gd_8 slabs in the (120) plane, as shown in Figure 3a,b, and Ru1-centered bonding units propagating in the *a*−*c* plane, as shown in Figure 3c,d. It should be noted that (120) was the typical cleavage plane in all measured samples. The planar interpenetrating framework (Figure 3b) has two-fold symmetry in the *c*-direction and is centered about Sn2. The central Sn2 is bonded to four Sn4 atoms at 3.093(1) Å, with each Sn4 atom bonded to one Sn10 at 2.961(1) Å and an adjacent Sn4 at 2.924(1) Å, all within the range of typical stannide-containing intermetallic compounds (*vide infra*). The Sn2−Sn4−Sn10 atoms form a planar web bonded to two Ru1 bonding units (one at each end of the web) with a Ru1−Sn10 (×4) bond distance of 2.734(1) Å. The Ru1 five-coordinate environment, as shown in Figure 3c, consists of Sn6, Sn11, Sn10, Sn5, and Sn3 atoms with bond distances in the range of 2.724(1)−2.811(1) Å. A short Sn3−Sn5 bond distance of 2.800(1) Å is present between two Ru1 bonding units. Ru1 environments always appear in pairs parallel to the *c*-axis (Figure 3c,d) with a Ru−Ru interatomic distance of 2.924(1) Å. This interatomic distance is longer than typical intermetallic Ru−Ru distances of 2.57−2.79 Å[26−28] but similar to the sum of the Ru−Ru covalent radii (2.92 Å),[29] suggesting a weak Ru−Ru interaction. A Sn12 atom connects three Ru1-centered pairs, shown in Figure 3d, by 1× Sn12−Sn6 (3.020(7) Å) and 2× Sn12−Sn11 (2.983(9) Å). There are 4 + 2 nearest-neighbor Ru1 pairs to a central Ru1-centered pair, four nearest-neighbor Ru1 pairs (shown in Figure 3d as polyhedra) either above or below the *a*−*c* plane and two next nearest-neighbor pairs on the same *a*−*c* plane (not shown), parallel to the *c*-axis. A 14-coordinate Gd4 atom, which is unique in that it is the only rare earth situated within the Ru−Sn/Sn−Sn bonding framework, is situated between three Ru-centered pairs (Figure 3d). The Gd4 coordination environment is Gd@$Gd_4Sn_8Ru_2$ (not shown). The symmetry of the Ru−Sn/Sn−Sn framework can be regenerated by translating one-half in both the *a*- and *c*-directions and mirroring in the *b*-direction.

The Gd-rich slabs, shown in Figure 4f, are composed of face-sharing (confacial) Sn1@Gd_8 distorted square antiprisms (Figure 4a), confacial Sn8@Gd_8 distorted square antiprisms (Figure 4b), confacial Sn7@Gd_8 square antiprisms (Figure 4c), and Sn9@Gd_8 bicapped trigonal prisms (Figure 4d). A similar Sn-centered confacial square antiprismatic arrangement is found in the Zintl phases $Yb_{36}Sn_{23}$[23] and $Ca_{31}Sn_{20}$.[24] Select Sn−Gd interatomic distances are provided in Table 3. Confacial Sn1, Sn7, and Sn8 polyhedra will herein be described as single units. The polyhedra-containing slabs form sheets from two alternating units when viewed in the *c*-direction,

Table 3. Interatomic Distances of the Sn1, Sn7, Sn8, and Sn9-Centered Polyhedra

$Gd_{30}Ru_{4.92}Sn_{30.54}$		$Tb_{30}Ru_{6.0}Sn_{29.5}$		$Dy_{30}Ru_{4.57}Sn_{30.7}$	
Sn1−Gd8 (×2)	3.104(1)	Sn1−Tb8 (×2)	3.087(1)	Sn1−Dy8 (×2)	3.068(1)
Sn1−Gd2 (×2)	3.140(1)	Sn1−Tb2 (×2)	3.141(1)	Sn1−Dy2 (×2)	3.115(1)
Sn1−Gd3 (×2)	3.293(1)	Sn1−Tb3 (×2)	3.259(1)	Sn1−Dy3 (×2)	3.265(1)
Sn1−Gd10 (×2)	3.296(1)	Sn1−Tb10 (×2)	3.316(1)	Sn1−Dy10 (×2)	3.247(1)
Sn1−Sn1	3.203(2)	Sn1−Sn1	3.168(2)	Sn1−Sn1	3.211(2)
Sn7−Gd8 (×2)	3.205(1)	Sn7−Tb8 (×2)	3.184(1)	Sn7−Dy8 (×2)	3.168(1)
Sn7−Gd7 (×2)	3.270(1)	Sn7−Tb7 (×2)	3.253(1)	Sn7−Dy7 (×2)	3.235(1)
Sn7−Gd5 (×2)	3.367(1)	Sn7−Tb5 (×2)	3.337(1)	Sn7−Dy5 (×2)	3.333(1)
Sn7−Gd6	3.427(1)	Sn7−Tb6	3.426(1)	Sn7−Dy6	3.370(1)
Sn7−Gd6	3.504(1)	Sn7−Tb6	3.516(1)	Sn7−Dy6	3.456(1)
Sn8−Gd10 (×2)	3.173(1)	Sn8−Tb10 (×2)	3.123(1)	Sn8−Dy10 (×2)	3.149(1)
Sn8−Gd1	3.301(1)	Sn8−Tb1	3.231(1)	Sn8−Dy1	3.257(1)
Sn8−Gd8 (×2)	3.328(1)	Sn8−Tb8 (×2)	3.317(1)	Sn8−Dy8 (×2)	3.281(1)
Sn8−Gd8 (×2)	3.383(1)	Sn8−Tb8 (×2)	3.390(1)	Sn8−Dy8 (×2)	3.353(1)
Sn8−Gd6	3.441(1)	Sn8−Tb6	3.347(1)	Sn8−Dy6	3.411(1)
Sn8−Sn8	2.964(2)	Sn8−Sn8	3.038(1)	Sn8−Sn8	2.930(2)
Sn8−Sn12	3.179(5)	Sn8−Ru12	3.100(1)	Sn8−Sn12	3.174(8)
Sn9−Gd5	3.079(1)	Sn9−Tb5	3.056(1)	Sn9−Dy5	3.052(1)
Sn9−Gd6	3.087(1)	Sn9−Tb6	3.076(1)	Sn9−Dy6	3.060(1)
Sn9−Gd10	3.088(1)	Sn9−Tb10	3.069(1)	Sn9−Dy10	3.056(1)
Sn9−Gd9	3.251(1)	Sn9−Tb9	3.227(1)	Sn9−Dy9	3.217(1)
Sn9−Gd11	3.271(2)	Sn9−Tb11	3.250(1)	Sn9−Dy11	3.238(1)
Sn9−Gd7	3.287(1)	Sn9−Tb7	3.266(1)	Sn9−Dy7	3.248(1)
Sn9−Gd3	3.319(1)	Sn9−Tb3	3.286(2)	Sn9−Dy3	3.305(1)
Sn9−Gd8	3.554(1)	Sn9−Tb8	3.517(1)	Sn9−Dy8	3.518(1)

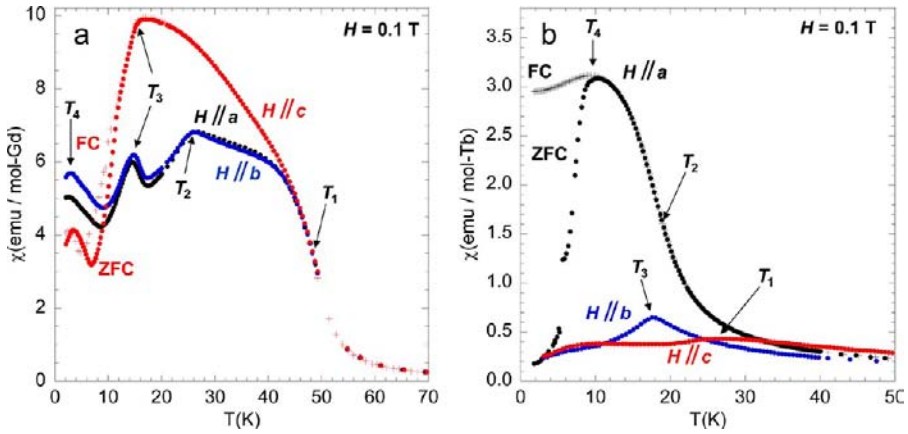

Figure 5. Temperature-dependent magnetic susceptibility of (a) $Gd_{30}Ru_{4.92}Sn_{30.54}$ from 2−70 K and of (b) $Tb_{30}Ru_6Sn_{29.5}$ from 2−50 K in an applied field of 0.1 T with $H \parallel a, b, c$ shown in black, blue, and red, respectively. FC and ZFC data are shown with $H \parallel c$ for $Gd_{30}Ru_{4.92}Sn_{30.54}$ and with $H \parallel a$ for $Tb_{30}Ru_6Sn_{29.5}$. ZFC data are shown in the remaining directions. Arrows highlight the magnetic transition temperatures.

shown in Figure 4e, which extend infinitely in the a−c plane. The first unit is composed of confacial Sn7 polyhedra which are triangular face sharing with four Sn9 polyhedra in a square planar configuration along the confacial equatorial plane of the two Sn7 polyhedra. These units are connected along the c-direction with edge-sharing Sn9 polyhedra (×4) by two adjacent units which form gaps shown in Figure 4f, allowing the Ru−Sn/Sn−Sn framework to penetrate between slabs. The second unit is constructed of confacial Sn1 polyhedra which are triangular face sharing (×4) with two sets of axially oriented confacial Sn8 polyhedra. The confacial plane of the Sn1 polyhedral units connects these units in the c-direction. The two sheets of alternating units are bridged by the Sn1 and Sn8 polyhedra of the second alternating unit. Confacial Sn1 polyhedra link the sheets by triangular face sharing (×4) with four Sn9 polyhedra and corner sharing (×4) with four Sn7 polyhedron. Sn8 confacial polyhedra bridge the sheets by triangular face sharing (×4) with four Sn9 polyhedra and by triangular face sharing (×2) with two sets of Sn7 confacial polyhedra. A more detailed description of the polyhedral environments can be found in the SI.

Stannide Bonding. Differentiation of the Sn environments in the Ru−Sn/Sn−Sn framework and in the Gd-rich slabs was conducted by carefully examining the Sn−Sn interatomic distances and the general coordination environments of each Sn atom. The Sn−Sn interatomic distances can be grouped into those with shorter interatomic distances (2.800−3.093 Å) and those with interatomic contacts >3.1 Å. The Sn3−Sn5 bond distance of 2.800(1) represents the shortest Sn−Sn interatomic distance, similar to that of elemental α-Sn (2.810 Å),[30]

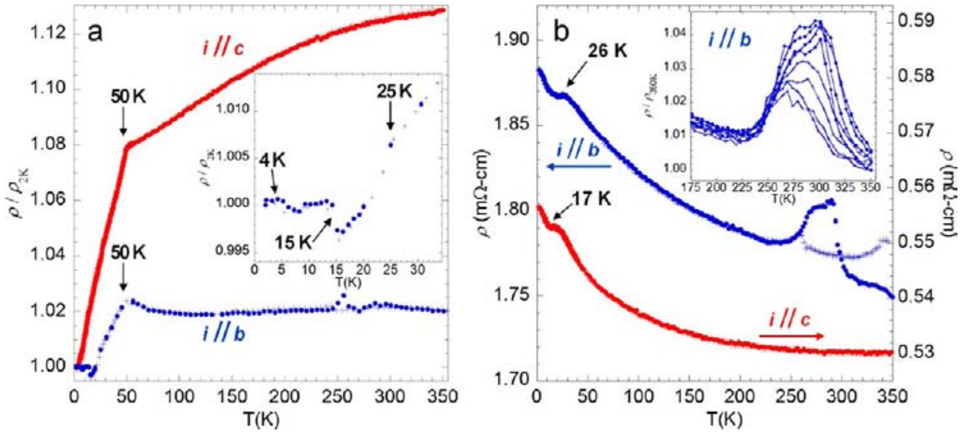

Figure 6. Temperature-dependent (a) resistivity of $Gd_{30}Ru_{4.92}Sn_{30.54}$ normalized to the resistivity at 2 K and (b) electrical resistivity of $Tb_{30}Ru_6Sn_{29.5}$ from 2−350 K with $i \parallel b$ (blue) and c (red). Arrows highlight anomalies in the electrical resistivity. The inset of (a) shows the low-temperature electrical resistivity of $Gd_{30}Ru_{4.92}Sn_{30.54}$ with $i \parallel b$, and the inset of (b) highlights the anomaly centered at ∼280 K of a second crystal of $Tb_{30}Ru_6Sn_{29.5}$ with $i \parallel b$, normalized to the resistivity at 350 K.

indicating strong Sn−Sn bonding interactions. The additional Sn−Sn bonds (2.924−3.093 Å) fall within the range of 2.819−3.117 Å for Sn−Sn contacts in the polar intermetallic compounds $Yb_4Mn_2Sn_5$ and Yb_3CoSn_6,[31] the strongly bonded Sn−Sn zigzag chains in Gd_4RuSn_8,[32] and the short Sn−Sn distances in Ru_3Sn_7.[33] The Sn atoms with Sn−Sn nearest interatomic distances >3.1 Å (Sn1, Sn7, and Sn9) and those which form singular dimers (Sn8) constitute the second Sn environment. These Sn atoms are all coordinated by 8 Gd atoms. The Sn8−Sn8 interatomic distance of 2.964(2) Å corresponds well to the Sn−Sn dimer distances in the Zintl phases Li_7Sn_2 (2.999(7) Å)[34] and $Ca_{31}Sn_{20}$ (3.158(2) Å).[24] The nearest Sn−Sn interatomic distances of Sn1, Sn7, and Sn9 are all >3.17 Å, and the $Sn@Gd_8$ square antiprismatic environments are similar to those of the isolated Sn atoms in the Zintl phases $Ca_{31}Sn_{20}$[24] and La_4Ge_3,[35] where isolated $(Ge/Sn)^{4-}$ and dimer $(Ge/Sn)_2^{6-}$ anions are surrounded by Ca and La cations, respectively. Thus, the Sn1, Sn7, Sn8, and Sn9 atoms of the title compounds likely carry some anionic character. The Sn8 atom, therefore, should be considered as a $1b-Sn^{3-}$ anion, and the Sn1, Sn7 and Sn9 atoms as $0b-Sn^{4-}$ anions. An interesting note regarding the confacial Sn-centered polyhedra is that the Sn8−Sn8 and Sn1−Sn1 distances of the Gd and Dy analogues (Table 3) are similar to one another, and those of the Tb analogue are longer (by ∼0.09 Å) and shorter (by ∼0.04 Å) than the Gd and Dy analogues, respectively, suggesting a change in bonding character of the Tb analogue relative to those of Gd and Dy.

Magnetization. Temperature-dependent magnetic susceptibility data with $H \parallel$ *a*-, *b*-, and *c*-directions are shown in Figures 5 and 6. Zero-field-cooled (ZFC) and field-cooled (FC) data were taken with $H \parallel a$, *b*, and *c* in $Gd_{30}Ru_{4.92}Sn_{30.54}$ (Figure S1) and $H \parallel a$ in $Tb_{30}Ru_6Sn_{29.5}$ to test for ZFC and FC divergence, indicative of ferromagnetic (FM) ordering, due to the large increase in susceptibility in these directions. Curie temperatures (T_C) are determined by the local minimum in the first derivative of magnetic susceptibility ($d\chi/dT$) as a function of temperature (Figure S1d).

Figure 5a shows the temperature-dependent magnetic susceptibility data of single crystal $Gd_{30}Ru_{4.92}Sn_{30.54}$ with H = 0.1 T $\parallel$ *a*, *b*, and *c*. $Gd_{30}Ru_{4.92}Sn_{30.54}$ displays a complex anisotropic magnetic behavior with a minimum of four temperature-dependent magnetic transitions from 49 to 3.5 K. A large increase in susceptibility is observed starting at 52 K in all three applied field directions. A small divergence in the ZFC and FC data is observed ∼42 K with $H \parallel a$ (Figure S1a), indicating ferromagnetic ordering with T_1 = 49 K. However, only ∼1 μ_B/Gd is observed at the apparent saturation point at 42 K (calculated by normalizing the temperature-dependent FC magnetization value to μ_B/Gd), suggesting a FM sublattice involving ∼15% of the Gd positions. It is worth noting that a broad feature in susceptibility, which occurs only with $H \parallel c$ beginning at 40 K with a maximum at 17 K, is likely a spin reorientation. The first antiferromagnetic (AFM) transition is apparent with $H \parallel a$ and *b* at T_2 = 26 K, and the second AFM transition occurs with $H \parallel a$, *b*, and *c* at T_3 ∼ 15 K. At 9 and 5.5 K, the magnitude of the FC data (Figure S1) drops below that of the ZFC data with $H \parallel b$ and *c*, respectively. Additionally, in all measured directions the magnitude of the susceptibility drops below that of the FM ordering at T_1, and a thermal hysteresis appears in the ZFC and FC minima, indicating a reorientation of the FM sublattices. The reorientation of the FM sublattices concomitant with the anomalous ZFC/FC behavior in both the Gd and Tb (*vide infra*) analogues may indicate a low-temperature structural transition. Another slope change is apparent with $H \parallel b$ and *c*, indicating a final AFM transition at T_4 = 3.5 K.

It is interesting that the field-dependent magnetization with $H \parallel a$, *b*, and *c* at 3 K, shown in Figure S2, appears isotropic and displays no hysteretic behavior. In all directions field-dependent magnetization saturates at ∼1.9 μ_B/Gd at 0.4 T, followed by a linear field dependence up to 9 T, suggesting an isotropic soft ferromagnetic sublattice and a paramagnetic (PM) sublattice, respectively.

Figure 5b shows the temperature-dependent magnetic susceptibility data of single crystal $Tb_{30}Ru_{46}Sn_{29.5}$ with H = 0.1 T $\parallel$ *a*, *b*, and *c*. $Tb_{30}Ru_{46}Sn_{29.5}$ also displays complex anisotropic magnetic ordering with four distinct ordering temperatures. An antiferromagnetic transition occurs with $H \parallel c$ at T_1 = 26.5 K, followed by a second AFM transition with $H \parallel b$ at T_3 = 17.5 K. A large increase in susceptibility occurs with $H \parallel a$ beginning at 24 K, and a divergence occurs in the ZFC and FC data at 11.5 K, indicating ferromagnetic ordering with T_2 = 19 K. A magnetic moment of 0.56 μ_B/Tb is observed at the maximum value of the temperature-dependent FC susceptibility with $H \parallel a$, suggesting the FM sublattice at T_2

involves only ~6% of the total Tb moment. A maximum occurs in the ZFC and FC data with $H \parallel a$, indicating an AFM transition at $T_4 = 10$ K, accompanied by a sharp drop in the ZFC data, similar to that of the Gd analogue, suggesting a reordering of the FM sublattice. This behavior may be caused by a low-temperature structural transition, as suggested with the Gd analogue, or a spin reorientation. Further measurements are in progress to ascertain the origin of this anomaly.

The field-dependent magnetization of $Tb_{30}Ru_6Sn_{29.5}$ at 3 K with $H \parallel a$, b, and c is shown in Figure S3. All three directions display field-dependent hysteresis; however, the hysteresis loops with $H \parallel b$ and c are elongated in field, whereas the loop with $H \parallel a$ displays hysteresis characteristics of a typical ferromagnetic sublattice with a coercive field of 0.35 T. The remnant magnetization with $H \parallel a$ is 0.55 μ_B/Tb, far from the theoretical saturated magnetization value 9.72 μ_B/Tb. This suggests that ~6% of the Tb sites are involved in the ferromagnetic sublattice, similar to the value determined from the maximum in the temperature-dependent magnetization. At fields higher than the convergence in the hysteresis loops in all applied field directions, the field-dependent magnetization becomes linear up to 9 T, suggesting the coexistence of ferromagnetic and paramagnetic sublattices at 3 K.

Temperature-dependent magnetic susceptibility data were fit with the modified Curie–Weiss (MCW) equation $\chi = \chi_o + C/(T - \theta_{CW})$, where χ_o is the temperature-independent contribution to the susceptibility, C is the Curie constant, and θ_{CW} is the Curie–Weiss temperature. Data were fit according to the criteria below. The inverse susceptibility of the Gd analogue in all directions shows nonlinearity below 173 K ($H \parallel a$) and ~148 K ($H \parallel b$, c). Nonlinearity is also present in the inverse susceptibility of the Tb analogue below ~199 K ($H \parallel a$) and ~92 K ($H \parallel b$, c); thus, data were fit above these temperatures. FC data were fit where available, as the inverse susceptibility of these data deviated less from linearity than the ZFC data. Values of μ_{eff}, χ_o, and θ_{CW} as well as fit ranges are shown in Tables 4a and 4b.

Table 4a. Curie Weiss Law Fit Values of μ_{eff}, χ_o, and θ_{CW} and Fit Ranges for $Gd_{30}Ru_{4.92}Sn_{30.54}$

$Gd_{30}Ru_{4.92}Sn_{30.54}$	$H \parallel a$	$H \parallel b$	$H \parallel c$
χ_0 (10^{-3} emu/mol·Ln)	1.1(8)	0.96(4)	0.26(4)
θ_{CW} (K)	21(4)	26(2)	25(2)
μ_{eff} (μ_B/Ln)	7.9(2)	7.81(7)	7.86(8)
fit range (K)	174–296	149–290	158–296

Table 4b. Curie Weiss Law Fit Values of μ_{eff}, χ_o, and θ_{CW} and Fit Ranges for $Tb_{30}Ru_6Sn_{29.5}$

$Tb_{30}Ru_6Sn_{29.5}$	$H \parallel a$	$H \parallel b$	$H \parallel c$
χ_0 (10^{-3} emu/mol·Ln)	0.7(4)	5.7(3)	4.6(2)
θ_{CW} (K)	−5.7(3)	−9.1(7)	10.3(3)
μ_{eff} (μ_B/Ln)	9.58(1)	9.44(4)	9.88(3)
fit range (K)	200–390	93–290	96–285

The μ_{eff} values obtained from the MCW fits are close to the theoretical values of 7.94 μ_B/Gd and 9.72 μ_B/Tb. The χ_o values from the fits are all small and positive, consistent with a small Pauli paramagnetic contribution from itinerant electrons in a low-resistivity material. The θ_{CW} temperatures in the Gd analogue, as determined from the fits, are all positive, suggesting dominant ferromagnetic correlations. Although it is clear that multiple magnetic sublattices are present in $Gd_{30}Ru_{4.92}Sn_{30.54}$, the ferromagnetic sublattice appears to be the most energetically favorable as $T_{C1} \sim 49$ K with $H \parallel a$, b, and c. The θ_{CW} temperatures of $Tb_{30}Ru_6Sn_{29.5}$ from the fit show a high degree of anisotropy with field direction. The negative θ_{CW} temperatures with $H \parallel a$ and b are consistent with the antiferromagnetic ordering observed in these directions, though FM characteristics are also observed with $H \parallel a$ in the temperature- and field-dependent magnetization but only correspond to a small percentage of the total Tb moment. The fitted θ_{CW} temperature with $H \parallel c$, however, is positive, while the temperature-dependent magnetization clearly shows AFM ordering with no indication of ferromagnetism. The Tb atoms in $Tb_{30}Ru_4Sn_{29.5}$ all have low site symmetry, and similar anisotropic θ_{CW} behavior has been observed in $Nd_2Ti_2O_7$ and attributed to contributions from crystal electric field effects due to the low Nd site symmetry.[36] Thus, the observed anisotropic θ_{CW} temperatures may be CEF mediated.

Resistivity. Figure 6 shows electrical transport of single crystals of $Gd_{30}Ru_{4.92}Sn_{30.54}$ and $Tb_{30}Ru_6Sn_{29.5}$ as a function of temperature from 2–350 K with the current (i) $\parallel b$ and c. Oriented single crystals of the Gd analogue were irregularly shaped; hence, resistivity normalized to the resistivity at 2 K (ρ/ρ_{2K}) is shown in Figure 6a. However, single crystals of the Tb analogue were large enough to polish to a bar shape with an estimated error in the resistivity due to geometric considerations with $i \parallel b$ and c of <20% and <10%, respectively. The resistivity (ρ) of two crystals of the Tb analogue was measured, which produced similar results; thus, ρ data for the crystal selected for thermal transport measurements are shown in Figure 6b. Warming (solid circles) and cooling (crosses) cycles are shown for both analogues.

$Gd_{30}Ru_{4.92}Sn_{30.54}$ and $Tb_{30}Ru_6Sn_{29.5}$ display a large degree of electric transport anisotropy in the form of temperature-dependent behavior and absolute magnitude, respectively. Above the magnetic ordering temperatures, the temperature-dependent curve of $Gd_{30}Ru_{4.92}Sn_{30.54}$ with $i \parallel c$ exhibits characteristics of a poor metal up to ~350 K, while the curve with $i \parallel b$ displays semiconducting-like, nearly temperature-independent behavior. While $Tb_{30}Ru_6Sn_{29.5}$ exhibits semiconducting-like behavior in both directions, the change in resistivity from 2 to 350 K is −7.63% with $i \parallel b$ and −4.72% with $i \parallel c$. Therefore, the temperature dependence of both analogues consistently displays more pronounced semiconducting behavior with $i \parallel b$ relative to $i \parallel c$. The low-temperature resistivity data for $Gd_{30}Ru_{4.92}Sn_{30.54}$ (highlighted in Figure 6a, inset) show slope changes at 50, 25, 15, and 4 K, while $Tb_{30}Ru_6Sn_{29.5}$ (highlighted in Figure 6b) displays slope changes at 26 and 17 K. These data correspond well to the magnetic ordering temperatures found from the temperature-dependent susceptibility data and are likely due to a reduction of spin-disorder scattering from the ordered magnetic moments. An anomaly with $i \parallel b$ is observed in the high-temperature resistivity of the Tb analogue centered at ~275 K. It is worth noting that a small anomaly is also present in the electrical resistivity of $Gd_{30}Ru_{4.92}Sn_{30.54}$ with $i \parallel b$, centered at ~255 K. To ascertain whether the anomaly in $Tb_{30}Ru_6Sn_{29.5}$ is intrinsic to the material, the resistance of another single crystal of $Tb_{30}Ru_6Sn_{29.5}$ was swept from low to high temperature and back several times and is shown in the inset of Figure 6b as resistivity normalized to the resistivity at 350 K. The results show that the anomaly is intrinsic. While the origin of this anomaly is still under investigation, it may be linked to the

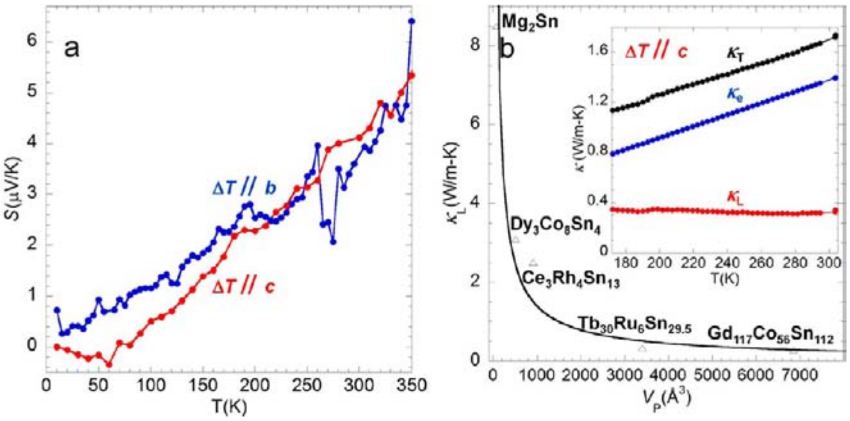

Figure 7. (a) Temperature-dependent thermopower of $Tb_{30}Ru_6Sn_{29.5}$ from 10−350 K with $i \parallel b$ (blue) and c (red), and (b) primitive volume (V_P) dependent lattice thermal conductivity of various stannides fit to a power law. Lattice thermal conductivity data for Mg_2Sn, $Dy_3Co_8Sn_4$, $Ce_3Rh_4Sn_{13}$, and $Gd_{117}Co_{56}Sn_{112}$ are obtained from refs 17 and 40−42, respectively. (b) Inset shows temperature-dependent total (black), electronic (blue), and lattice (red) thermal conductivity of $Tb_{30}Ru_6Sn_{29.5}$ from 172−305 K with $\Delta T \parallel c$.

magnetism of the material, as the inverse susceptibility of $Tb_{30}Ru_6Sn_{29.5}$ deviates from linearity at high temperatures (~200 K) relative to the highest magnetic ordering temperature observed at $T_1 = 26.5$ K.

The temperature-dependent resistivity data of $Tb_{30}Ru_6Sn_{29.5}$ with $i \parallel b$ and c show semiconducting-like behavior with largely different magnitudes. The room temperature resistivity values are 1.77 and 0.53 mΩ·cm with $i \parallel b$ and c, respectively; therefore, the resistivity anisotropy (ρ_b/ρ_c) is 3.34 at 300 K. Bulk three-dimensional (3D) solids typically display low resistivity anisotropy of ~1, but some exceptions are present in the literature, such as the high-temperature Kondo systems URu_2Si_2 and $CePt_2In_7$ with resistivity anisotropies of ~1.94 and ~3.3, respectively, at 300 K,[13,14] and the open 3D framework $CaFe_4As_3$ shows a room temperature anisotropic resistivity ~1.3.[16] Quasicrystalline approximant phases, such as T-$Al_{72.5}Mn_{21.5}Fe_{6.0}$ and d-Al−Co−Ni, have been shown to exhibit resistivity anisotropies of 1.23 and 8.4, respectively.[11,12] On the other hand, 2D materials have been shown to exhibit very high resistivity anisotropy, such as the layered superconductor $BaFe_2As_2$ with $\rho_c/\rho_{ab} \sim 150$.[15] Thus, with $\rho_b/\rho_c = 3.34$, $Tb_{30}Ru_6Sn_{29.5}$ displays one of the highest anisotropic resistivity values ever reported in a 3D extended solid system.

Thermopower. Figure 7a shows the thermopower as a function of temperature of $Tb_{30}Ru_6Sn_{29.5}$ with $\Delta T \parallel b$ and c from 10−350 K. Both directions show positive thermopower at 300 K with a positive temperature dependence. The thermopower with $\Delta T \parallel c$ is slightly negative from 10−60 K with a negative temperature coefficient and then becomes positive with a positive temperature coefficient above 60 K, indicating a mixture of n- and p-type charge carriers. The thermopower with $\Delta T \parallel b$ is positive across the entire measured temperature range with a positive temperature coefficient, indicating dominant p-type carrier conduction. There is an anomaly with $\Delta T \parallel b$ centered at ~270 K, which corresponds to an anomaly in the electrical resistivity with $i \parallel b$; however, there is no evidence of the anomaly in the thermopower data with $\Delta T \parallel c$, which mirrors the behavior of the electrical resistivity data. The slopes of the temperature dependence of the thermopower are clearly different in the two measured directions, and the two temperature-dependent curves cross at ~250 K, indicating that the thermopower also displays anisotropic behavior. This suggests that the electronic structure is highly anisotropic and that the difference in magnitude of the electrical resistivity is likely due to a highly anisotropic Fermi surface similar to $PdCoO_2$[37] rather than the anisotropic quenched defect scattering mechanism dominant in the quasicrystalline approximant T-$Al_{72.5}Mn_{21.5}Fe_{6.0}$.[11]

Thermal Conductivity. The inset of Figure 7b shows the total (κ_T), electronic (κ_e), and lattice (κ_L) thermal conductivity as a function of temperature of $Tb_{30}Ru_6Sn_{29.5}$ with $\Delta T \parallel c$ from 172−305 K. κ_e is calculated using the Wiedemann−Franz law $\kappa_e = L_o T/\rho$, where $L_o = 2.44 \times 10^{-8}$ W·Ω/K^2 is the Lorenz number and ρ is the electrical resistivity obtained from the same crystal with $i \parallel c$. The lattice thermal conductivity is calculated using $\kappa_T = \kappa_L + \kappa_e$. κ_T steadily increases over the entire measured temperature range, while κ_L decreases as a function of temperature as expected. The lattice thermal conductivity of $Tb_{30}Ru_6Sn_{29.5}$ at 300 K is exceptionally low with $\kappa_L = 0.33$ W/m·K. The low room temperature κ_L value of $Tb_{30}Ru_6Sn_{29.5}$ can be explained by the sizable volume of the primitive unit cell. Reduction of lattice thermal conductivity as a function of primitive unit cell volume (V_P) in systems with similar average atomic mass and bonding characteristics is a well-documented phenomenon, both theoretically[38] and experimentally,[39] which typically scales as $\sim 1/V_P$. Figure 7 shows the room temperature κ_L values of $Tb_{30}Ru_6Sn_{29.5}$ and other stannides as a function of V_P. Similar to a study conducted on complex antimonides,[39] the data are fit to a power law of $\kappa_L = 415 \cdot V_P^{-0.82}$. The room temperature κ_L value of $Tb_{30}Ru_6Sn_{29.5}$ is clearly situated below the curve fit. The deviation of $Tb_{30}Ru_6Sn_{29.5}$ from the fit may be due to the large degree of disorder modeled in the system, which has been shown to significantly lower lattice thermal conductivity.[38] The observation of such a low lattice thermal conductivity in $Tb_{30}Ru_6Sn_{29.5}$, concomitant with the highly anisotropic nature of the electrical resistivity, introduces the potential of highly anisotropic thermal conductivity. Though our sample was not large enough for anisotropic thermal conductivity measurements, the anisotropic thermal conductivity can be estimated using the anisotropic resistivity values and assuming an isotropic κ_L. At room temperature $\kappa_T \parallel c$ is 1.7 W/m·K, and a simple calculation yields $\kappa_T \parallel b$ of 0.74 W/m·K, with a theoretical thermal transport anisotropy of ~2.4.

■ CONCLUSIONS

$Gd_{30}Ru_{4.92}Sn_{30.54}$, $Tb_{30}Ru_6Sn_{29.5}$, and $Dy_{30}Ru_{4.57}Sn_{30.72}$ adopt a new structure type with 24 atomic positions and a large V_P. The structure of $Gd_{30}Ru_{4.92}Sn_{30.54}$ consists of a unique combination of slabs of Sn@Gd_8 polyhedra and an interpenetrating Sn-based framework. The slabs and framework are considered to be more ionic and covalent in nature, respectively. Furthermore, disorder was modeled in the system with two independent scenarios based on the presence or absence of the Ru2′ position. This disorder may affect the physical properties observed in the system.

$Gd_{30}Ru_{4.92}Sn_{30.54}$ and $Tb_{30}Ru_6Sn_{29.5}$ both display highly anisotropic magnetic and transport properties. The temperature-dependent magnetism fits a modified Curie−Weiss law with the fit magnetic moments corresponding well to the expected moments for Gd and Tb in all measured directions. The temperature-dependent magnetism also shows anisotropic low-temperature behavior with at least four magnetic transitions in $Gd_{30}Ru_{4.92}Sn_{30.54}$ and four magnetic transitions in $Tb_{30}Ru_6Sn_{29.5}$. Field-dependent magnetism taken at 3 K suggests the presence of a ferromagnetic sublattice in both analogues. The electrical resistivity of $Gd_{30}Ru_{4.92}Sn_{30.54}$ and $Tb_{30}Ru_6Sn_{29.5}$ is highly anisotropic with an anisotropic resistivity ratio of 3.34 in $Tb_{30}Ru_6Sn_{29.5}$, one of the largest ever reported in a 3D extended solid. It is possible that the 2D-like Sn@Gd_8 slabs contribute to the observed electrical characteristics; further detailed studies of the material will be necessary to determine the nature of the electrical anisotropy. The presence of an anomaly at ∼275 K in both the electrical resistivity and thermopower of $Tb_{30}Ru_6Sn_{29.5}$ with i and $S \parallel b$, and the absence of this anomaly with i and $S \parallel c$, confirms its intrinsic and highly anisotropic nature. Additionally, the differing slope changes and general features of the thermopower between $S \parallel b$ and c imply that the anisotropic electrical characteristics are a result of a highly anisotropic Fermi surface; though, a small contribution from anisotropic quenched defect scattering is likely present due to the large degree of disorder present in the system.

The thermal conductivity of $Tb_{30}Ru_6Sn_{29.5}$ is low and dominated by the κ_e in the measured temperature range. The calculated κ_L of 0.33 W/m·K at 300 K is compared to other Sn-containing systems with various primitive lattice volumes. A theoretical anisotropic thermal conductivity ratio of 2.4 is calculated from the electrical resistivity data. This system displays a rare mixture of highly anisotropic and complex magnetism and transport properties certainly deserving future study. The anisotropic electrical and thermal properties may prove to be useful in technological applications where preferential thermal transport properties are desired, while the low-temperature magnetic phenomena observed may have magnetocaloric applications.

The title compounds exhibit a complex structure with concomitant complex properties, which were only discovered through careful structural characterization, postgrowth sample preparation, and a meticulous transfer of the structural orientation information to physical property measurement and analysis. We have presented an overview of $Ln_{30}Ru_{4+x}Sn_{31-x}$ (Ln = Gd and Tb), which crystallizes in a new structure-type and displays anisotropic magnetic and electrical properties, but further detailed magnetic and electrical characterization will be necessary to fully understand these phenomena. Materials displaying exotic properties are paving the way for new technologies, such as spintronics and magnetocalorics. Only with a thorough understanding of the structure−property relationships in complex systems will we be able to tune the properties of these materials in order to exploit them for application purposes.

■ ASSOCIATED CONTENT

Ⓢ Supporting Information

Details of atomic disorder refinement and description of the polyhedral Sn1, Sn7−Sn9 structural units; figures displaying detailed ZFC and FC temperature-dependent magnetic susceptibility of $Gd_{30}Ru_{4.92}Sn_{30.54}$, field-dependent magnetization of $Gd_{30}Ru_{4.92}Sn_{30.54}$, and field-dependent magnetization of $Tb_{30}Ru_6Sn_{29.5}$; tables of positions, occupancies, and atomic displacement parameters for $Gd_{30}Ru_{4.92}Sn_{30.54}$ and $Tb_{30}Ru_6Sn_{29.5}$. This information is available free of charge via the Internet at http://pubs.acs.org.

■ AUTHOR INFORMATION

Corresponding Author

jchan@lsu.edu

Notes

The authors declare no competing financial interest.

■ ACKNOWLEDGMENTS

J.Y.C. acknowledges Louisiana Board of Regents and NSF DMR 1063735, D.P.Y. acknowledges NSF DMR 1005764, R.J. acknowledges NSF DMR 1002622, and S.S. acknowledges NSF DMR 0545728 for funding. The authors acknowledge Luis Reyes, Bradford Fulfer, Gregory Morrison, and Frank Fronczek for useful discussion.

■ REFERENCES

(1) Giguere, A.; Foldeaki, M.; Gopal, B. R.; Chahine, R.; Bose, T. K.; Frydman, A.; Barclay, J. A. *Phys. Rev. Lett.* **1999**, *83*, 2262−2265.

(2) Canfield, P. C.; Bud'ko, S. L. *Sci. Am.* **2005**, *292*, 80−87.

(3) Rotter, M.; Tegel, M.; Johrendt, D. *Phys. Rev. Lett.* **2008**, *101*, 1−4.

(4) Phelan, W. A.; Menard, M. C.; Kangas, M. J.; McCandless, G. T.; Drake, B. L.; Chan, J. Y. *Chem. Mater.* **2012**, *24*, 409−420.

(5) Snyder, G. J.; Christensen, M.; Nishibori, E.; Caillat, T.; Iversen, B. B. *Nat. Mater.* **2004**, *3*, 458−463.

(6) Brown, S. R.; Kauzlarich, S. M.; Gascoin, F.; Snyder, G. J. *Chem. Mater.* **2006**, *18*, 1873−1877.

(7) Jiang, J.; Payne, A. C.; Olmstead, M. M.; Lee, H. O.; Klavins, P.; Fisk, Z.; Kauzlarich, S. M.; Hermann, R. P.; Grandjean, F.; Long, G. J. *Inorg. Chem.* **2005**, *44*, 2189−2197.

(8) Goforth, A. M.; Hope, H.; Condron, C. L.; Kauzlarich, S. M.; Jensen, N.; Klavins, P.; MaQuilon, S.; Fisk, Z. *Chem. Mater.* **2009**, *21*, 4480−4489.

(9) Zaharko, O.; Keller, L.; Ritter, C. *J. Magn. Magn. Mater.* **2002**, *253*, 130−139.

(10) Kim, M. S.; Sung, N. H.; Son, Y.; Ko, M. S.; Cho, B. K. *Appl. Phys. Lett.* **2011**, *98*, 1−3.

(11) Heggen, M.; Feuerbacher, M.; Ivkov, J.; Popcevic, P.; Batistic, I.; Smontara, A.; Jagodic, M.; Jaglicic, Z.; Janovec, J.; Wencka, M.; Dolinsek, J. *Phys. Rev. B* **2010**, *81*, 1−11.

(12) Bobnar, M.; Jeglic, P.; Klanjsek, M.; Jaglicic, Z.; Wencka, M.; Popcevic, P.; Ivkov, J.; Stanic, D.; Smontara, A.; Gille, P.; Dolinsek, J. *Phys. Rev. B* **2012**, *85*, 1−11.

(13) Palstra, T. T. M.; Menovsky, A. A.; Mydosh, J. A. *Phys. Rev. B* **1986**, *33*, 6527−6530.

(14) Tobash, P. H.; Ronning, F.; Thompson, J. D.; Scott, B. L.; Moll, P. J. W.; Batlogg, B.; Bauer, E. D. *J. Phys.: Condens. Matter* **2012**, *24*, 1−7.

(15) Wang, X. F.; Wu, T.; Wu, G.; Chen, H.; Xie, Y. L.; Ying, J. J.; Yan, Y. J.; Liu, R. H.; Chen, X. H. *Phys. Rev. Lett.* **2009**, *102*, 1−4.

(16) Karki, A. B.; McCandless, G. T.; Stadler, S.; Xiong, Y. M.; Li, J.; Chan, J. Y.; Jin, R. *Phys. Rev. B* **2011**, *84*, 1−6.

(17) Schmitt, D. C.; Haldolaarachchige, N.; Xiong, Y. M.; Young, D. P.; Jin, R. Y.; Chan, J. Y. *J. Am. Chem. Soc.* **2012**, *134*, 5965−5973.

(18) Bodak, O. P.; Gladyshe, Ei *Sov. Phys. Crystallogr.* **1970**, *14*, 859−861.

(19) Burla, M. C.; Carrozzini, B.; Cascarano, G. L.; Giacovazzo, C.; Polidori, G. *Z. Kristallogr.* **2002**, *217*, 629−635.

(20) Sheldrick, G. M. *Acta Crystallogr.* **2008**, *64*, 112−122.

(21) Spek, A. L. *Acta Crystallogr.* **2009**, *D65*, 148−155.

(22) Palenzona, A.; Manfrinetti, P.; Fornasini, M. L. *J. Alloys Comp.* **2000**, *312*, 165−171.

(23) Leon-Escamilla, E. A.; Corbett, J. D. *Inorg. Chem.* **1999**, *38*, 738−743.

(24) Ganguli, A. K.; Guloy, A. M.; Leonescamilla, E. A.; Corbett, J. D. *Inorg. Chem.* **1993**, *32*, 4349−4353.

(25) Fornasini, M. L.; Franceschi, E. *Acta Crystallogr.* **1977**, *33*, 3476−3479.

(26) Pöttgen, R.; Hoffmann, R. D.; Sampathkumaran, E. V.; Das, I.; Mosel, B. D.; Müllmann, R. *J. Solid State Chem.* **1997**, *134*, 326−331.

(27) Wu, Z. Y.; Hoffmann, R. D.; Pottgen, R. *Z. Anorg. Allg. Chem.* **2002**, *628*, 1484−1488.

(28) Riecken, J. F.; Al Alam, A. F.; Chevalier, B.; Matar, S. F.; Pottgen, R. *Z. Naturforsch Pt. B* **2008**, *63*, 1062−1068.

(29) Cordero, B.; Gomez, V.; Platero-Prats, A. E.; Reves, M.; Echeverria, J.; Cremades, E.; Barragan, F.; Alvarez, S. *Dalton Trans.* **2008**, 2832−2838.

(30) Emsley, J. *The Elements*, 2nd ed.; Oxford University Press: New York, 1991; p 251.

(31) Lei, X. W.; Zhong, G. H.; Li, M. J.; Mao, J. G. *J. Solid State Chem.* **2008**, *181*, 2448−2455.

(32) Francois, M.; Venturini, G.; Malaman, B.; Roques, B. *J. Less-Common Met.* **1990**, *160*, 197−213.

(33) Chakoumakos, B. C.; Mandrus, D. *J. Alloys Comp.* **1998**, *281*, 157−159.

(34) Frank, U.; Muller, W.; Schafer, H. *Z. Naturforsch Pt. B* **1975**, *B 30*, 6−9.

(35) Kauzlarich, S. M. *Chemistry, Structure, and Bonding of Zintl Phases and Ions*, 1st ed.; VCH Publishers, Inc.: New York, 1996; p 306.

(36) Xing, H.; Long, G.; Guo, H. J.; Zou, Y. M.; Feng, C. M.; Cao, G. H.; Zeng, H.; Xu, Z. A. *J. Phys.: Condens. Matter* **2011**, *23*, 1−6.

(37) Ong, K. P.; Singh, D. J.; Wu, P. *Phys. Rev. Lett.* **2010**, *104*, 1−4.

(38) Tritt, T. M. *Thermal Conductivity Theory, Properties and Applications*; Kluwer Academic: New York, 2004; p 290.

(39) Toberer, E. S.; May, A. F.; Snyder, G. J. *Chem. Mater.* **2010**, *22*, 624−634.

(40) Martin, J. J.; Danielson, G. C. *Phys. Rev.* **1968**, *166*, 879−882.

(41) Schwall, M.; Schoop, L. M.; Ouardi, S.; Balke, B.; Felser, C.; Klaer, P.; Elmers, H. J. *Adv. Funct. Mater.* **2012**, *22*, 1822−1826.

(42) Köhler, U. *Thermoelectric transport in rare-earth compounds*; University of Dresden: Dresden, 2007.